

Meteoric smoke and meteor influx from global SOFIE observations

Mark E. Hervig¹, John Maurice Campbell Plane², David E. Siskind³, Wuhu Feng², Charles Bardeen⁴, and Scott Martin Bailey⁵

¹GATS Inc.

²University of Leeds

³Naval Research Laboratory

⁴National Center for Atmospheric Research (UCAR)

⁵Virginia Polytechnic Institute and State University, Blacksburg, VA

November 22, 2022

Abstract

Measurements from the Solar Occultation For Ice Experiment (SOFIE) are used to characterize meteoric smoke and meteor influx in both hemispheres. New smoke extinction retrievals from sunrise measurements in the Northern Hemisphere (NH) are presented, which complement the previously reported sunset observations in the Southern Hemisphere (SH). The sunrise observations are in good agreement with simulations from the Whole Atmosphere Community Climate Model (WACCM), for both the seasonal and height dependence of smoke in the mesosphere. The SOFIE - WACCM comparisons assumed that smoke in the mesosphere exists purely as Fe-rich olivine. This is justified because olivine is detected optically by SOFIE, it has the same elemental abundance as incoming meteoroids, and it is anticipated by theory and laboratory experiments. Treating mesospheric smoke as olivine furthermore brings closure in terms of the ablated and total meteoric influx determined here from SOFIE and a recent and independent investigation based on models and observations. SOFIE observations from 2007 - 2021 indicate a global ablated meteoric influx of 7.3 ± 2.0 metric tons per day (t/d), which corresponds to a total influx (ablated plus surviving material) of 25.0 ± 7.0 t/d. Finally, SOFIE indicates less smoke in the polar winter SH compared to NH winter. Finally, the results indicate stronger descent in the NH polar winter mesosphere than in the SH winter. This hemispheric asymmetry is indicated by smoke and water vapor results from both SOFIE and WACCM.

1 **Meteoric smoke and meteor influx from global SOFIE observations**

2

3 **Mark E. Hervig¹, John M. C. Plane², Dave E. Siskind³, Wuhu Feng^{2,4}, Charles G.**
4 **Bardeen⁵, and Scott M. Bailey⁶.**

5 ¹GATS, Driggs, Idaho, USA.

6 ²School of Chemistry, University of Leeds, Leeds, UK.

7 ³Space Science Division, Naval Research Laboratory, Washington, DC, USA.

8 ⁴NCAS School of Earth and Environment, University of Leeds, Leeds, UK.

9 ⁵National Center for Atmospheric Research, Boulder, Colorado, USA.

10 ⁶Virginia Polytechnic Institute, Blacksburg, Virginia, USA.

11 Corresponding author: Mark Hervig (m.e.hervig@gats-inc.com)

12

13 **Main Points:**

14 1) The composition of smoke in the mesosphere is consistent with iron-rich olivine.

15 2) Global ablated meteoric influx is $7.3 \pm 2.0 \text{ t d}^{-1}$, with a total influx of $25.0 \pm 7.0 \text{ t d}^{-1}$.

16 3) Smoke and H₂O are consistent with stronger winter descent in the Northern mesosphere relative
17 to the South.

18

19 **Abstract.** Measurements from the Solar Occultation For Ice Experiment (SOFIE) are used to
20 characterize meteoric smoke and meteor influx in both hemispheres. New smoke extinction
21 retrievals from sunrise measurements in the Northern Hemisphere (NH) are presented, which
22 complement the previously reported sunset observations in the Southern Hemisphere (SH). The
23 sunrise observations are in good agreement with simulations from the Whole Atmosphere
24 Community Climate Model (WACCM), for both the seasonal and height dependence of smoke in
25 the mesosphere. The SOFIE - WACCM comparisons assumed that smoke in the mesosphere exists
26 purely as Fe-rich olivine. This is justified because olivine is detected optically by SOFIE, it has
27 the same elemental abundance as incoming meteoroids, and it is anticipated by theory and
28 laboratory experiments. Treating mesospheric smoke as olivine furthermore brings closure in
29 terms of the ablated and total meteoric influx determined here from SOFIE and a recent and
30 independent investigation based on models and observations. SOFIE observations from 2007 -
31 2021 indicate a global ablated meteoric influx of 7.3 ± 2.0 metric tons per day (t d^{-1}), which
32 corresponds to a total influx (ablated plus surviving material) of $25.0 \pm 7.0 \text{ t d}^{-1}$. Finally, SOFIE
33 indicates less smoke in the polar winter SH compared to NH winter. Finally, the results indicate
34 stronger descent in the NH polar winter mesosphere than in the SH winter. This hemispheric
35 asymmetry is indicated by smoke and water vapor results from both SOFIE and WACCM.

36 **1. Introduction**

37 A layer of meteoric smoke resides in the mesosphere and stratosphere, as nanometer sized
38 aerosol that results from the ablation of cosmic dust particles during atmospheric entry [*Plane et*
39 *al.*, 2012; *Hervig et al.*, 2017a]. Smoke in the mesosphere is enhanced during polar winter and
40 reduced in summer, due to transport by the global meridional mesospheric circulation. This
41 behavior was first predicted by a two-dimensional model [*Megner et al.*, 2008] and later observed
42 by the Solar Occultation for Ice Experiment (SOFIE) [*Hervig et al.*, 2009]. The annual variation
43 in smoke occurs despite the annual variation in meteoric influx (MI), which is highest (lowest)
44 near the fall (spring) equinox [*Fentzke et al.*, 2008]. The phase difference between smoke in the
45 middle atmosphere and meteoric influx is due to the dominance of transport in the mesosphere, as
46 discussed by *Bardeen et al.* [2008].

47 Estimates of the total meteoric influx (TMI, ablated plus surviving material) into Earth's
48 atmosphere have ranged from 1 to 270 metric tons per day (t d^{-1}) [e.g., *Plane*, 2012]. The most
49 recent results, however, appear to be converging on a narrower range ($30 - 60 \text{ t d}^{-1}$) than previously.
50 *Gardner et al.* [2014] report a TMI of $60 \pm 16 \text{ t d}^{-1}$ based on mid-latitude lidar observations of
51 sodium near the mesopause combined with models. *Carrillo-Sánchez et al.* [2016] derived a TMI
52 of $43 \pm 14 \text{ t d}^{-1}$ by combining a meteoric ablation model with a solar system dust model, constrained
53 by lidar measurements of the vertical fluxes of mesospheric Na and Fe at mid-latitudes and cosmic
54 spherule deposition at the South Pole. Importantly, they also found that only $\sim 18\%$ of the incoming
55 meteoric material is ablated (and thus resident in the middle atmosphere), far lower than previous
56 estimates ($>80\%$). *Hervig et al.* [2017a] used SOFIE satellite observations of meteor smoke in the
57 Southern Hemisphere (SH) mesosphere to derive a TMI of $30 \pm 18 \text{ t d}^{-1}$. Most recently, *Carrillo-*
58 *Sánchez et al.* [2020] report an update to the *Carrillo-Sánchez et al.* [2016] analysis (a new

59 chemical ablation model) which suggests $TMI = 28 \pm 16 \text{ t d}^{-1}$, and a slightly higher ablated fraction
60 (30%) than previously.

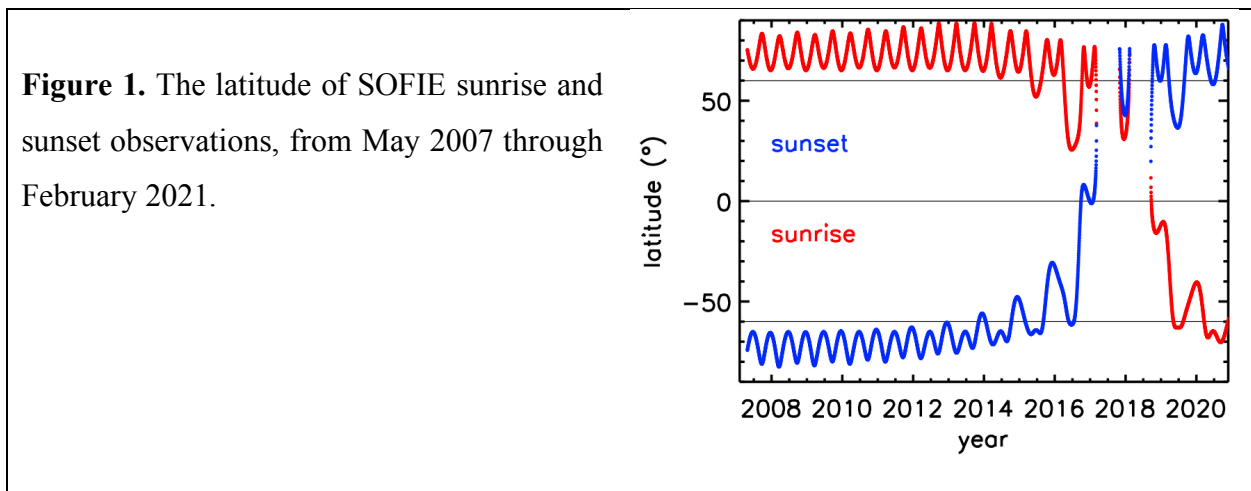
61 The present study uses SOFIE observations to examine the time and height dependence of
62 meteoric smoke in the Northern Hemisphere (NH), for the first time. This advance comes from
63 new methods for calibrating the detector response drift during sunrise, which has been more
64 challenging than for the sunset measurements. The new smoke results are compared to models and
65 to SOFIE sunset observations, and subsequently used to determine meteoric influx during 2007 -
66 2021 in both hemispheres.

67 **2. SOFIE Observations**

68 SOFIE has observed temperature, five gases (O_3 , H_2O , CO_2 , CH_4 , and NO), polar
69 mesospheric clouds (PMC), and meteoric smoke, from the Aeronomy of Ice in the Mesosphere
70 (AIM) satellite during 2007 - present [Russell *et al.*, 2009]. The occultation measurements are used
71 to conduct retrievals at altitudes from roughly 20 to 95 km (up to 150 km for NO), with a vertical
72 resolution of ~ 1.8 km. The measurement latitudes have evolved over the years, with dedicated
73 polar coverage from 2007 – 2016 and 2019 – present. The years from 2017 - 2019 had equatorial
74 coverage with some interruptions, and a change from sunsets (sunrise) in the SH (NH) to the NH
75 (SH), due to progression of the AIM orbit (Figure 1). The current SOFIE data is version 1.3 which
76 is available online (sofie.gats-inc.com).

77 The primary challenge in interpreting the meteoric smoke signals is accounting for a small
78 drift in detector responsivity, which occurs due to heating of the system during solar view. The
79 response drift is small (< 10 counts) compared to the dynamic range (2^{15} counts), but significant
80 in terms of the response due to meteoric smoke (< 20 counts). For sunset observations the drift is
81 highly linear, and is successfully removed by extrapolating a fit to measurements above the

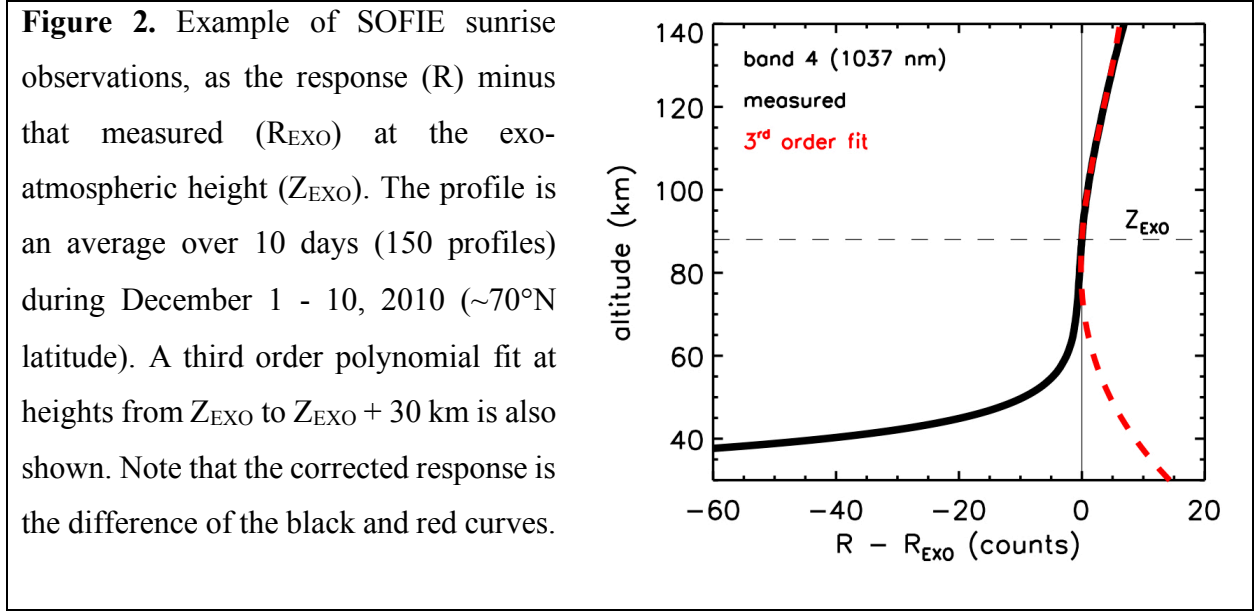
82 atmosphere (exo-atmospheric) to lower heights [Gordley *et al.*, 2009]. Results for sunset smoke
83 observations were first described by *Hervig et al.* [2009], who reported smoke extinction ($\beta(\lambda)$) at
84 1037 nm wavelength (λ). An updated response calibration approach [Hervig *et al.*, 2017a]
85 provided sunset smoke extinctions at the additional wavelengths of 330 and 867 nm, which
86 subsequently allowed the chemical composition of smoke to be identified. Sunset measurements
87 benefit from a long period of solar observation above the atmosphere, which allows the instrument
88 temperature to achieve a state of steady linear change, facilitating straightforward corrections to
89 the signals. The drift in sunrise measurements is more difficult to characterize, however, because
90 the atmosphere is observed before the instrument temperature has a chance to stabilize.



91

92 The drift in sunrise observations above the atmosphere was found to be consistent with a
93 third order polynomial. Attempting such a high-order fit to individual measurements can be
94 problematic, however, as variations due to noise can cause unrealistic values in the subsequent
95 extrapolation to atmospheric altitudes. This issue is eliminated when fitting a polynomial to the
96 average signal versus height based on multiple days (15 observations per day) as discussed in
97 *Hervig et al.* [2017a]. The results here used 10-day averages (150 profiles), as shown in the
98 example in Figure 2, where the response (R) minus the exo-atmospheric response (R_{EXO}) is shown

99 versus height. This approach was found to reduce the statistical uncertainty in the drift corrections
 100 to levels that were below both the statistical noise limit (~ 0.3 counts, see *Gordley et al.*, 2009) and
 101 the atmospheric response. The uncertainty in retrieved smoke extinction is defined as the root-
 102 sum-square of the measurement noise, drift correction uncertainty, and errors in removal of
 103 interference. Interference is due to O_3 absorption and Rayleigh scattering at 330 and 867 nm, and
 104 only Rayleigh at 1037 nm. As a result the 1037 nm observations have the lowest uncertainties, and
 105 are thus used here to determine meteoric influx.



106
 107 For this work meteoric smoke extinctions were retrieved using 10-day averages of SOFIE
 108 signals, for observations from 2007 - 2021. The signal averages used only measurements that were
 109 free of PMCs, which are opaque enough to overwhelm the signal due to smoke. For the new sunrise
 110 (NH) observations reported here, this results in a lack of smoke extinctions during June and July
 111 when PMCs are ubiquitous at polar latitudes. Similarly, SH smoke extinctions are rarely obtained
 112 during December - January.

113 SOFIE measurements of smoke extinction are converted to volume density (V) using the
114 relationship reported by *Hervig et al.* [2017a], $V = C \beta(1037)$, where C is a constant that varies
115 with smoke composition. This linear relationship exists because at the SOFIE wavelengths smoke
116 attenuation is entirely due to absorption, which is proportional to the particle radius cubed.
117 Obtaining estimates of V from SOFIE allows direct comparison with the models, and also provides
118 a means to determine meteoric influx. SOFIE multi-wavelength observations show that the most
119 likely (>60% detection probability) smoke compositions are magnesiowüstite ($\text{Mg}_x\text{Fe}_{1-x}\text{O}$, $x = 0,$
120 $0.1, 0.2,$ and 0.6) and iron-rich olivine ($\text{Mg}_{0.8}\text{Fe}_{1.2}\text{SiO}_4$) [*Hervig et al.*, 2017a]. Note that values of
121 C span roughly 250 to 1900 ($\mu\text{m}^3 \text{cm}^{-3} \text{km}$) for the potential smoke compositions. Furthermore,
122 the different compounds are identified simultaneously, due to their spectral similarity combined
123 with SOFIE uncertainties. Of the compounds indicated by SOFIE, only olivine has an elemental
124 makeup that is similar to the relative elemental abundances of ablated meteoric material (see Table
125 1). Furthermore, laboratory and theoretical studies suggest that iron-rich olivine should result from
126 the recombination of meteoric ablation products in the mesosphere [*Saunders and Plane*, 2011].
127 Taking these clues, the SOFIE extinctions were analyzed below assuming that smoke consists only
128 of $\text{Mg}_{0.8}\text{Fe}_{1.2}\text{SiO}_4$. The first consequence is that the conversion of extinction to volume density
129 becomes $V/\beta = 1512 \pm 1 \mu\text{m}^3 \text{cm}^{-3} \text{km}$. This is in contrast to the previous interpretation which used
130 the average V/β for the possible compositions ($687 \pm 470 \mu\text{m}^3 \text{cm}^{-3} \text{km}$), and accepted the large
131 standard deviation as an experimental uncertainty [*Hervig et al.*, 2017a]. Note that the resulting
132 SOFIE V (and MI) are increased here by a factor of ~ 2 compared to previous results. The second
133 consequence of assuming $\text{Mg}_{0.8}\text{Fe}_{1.2}\text{SiO}_4$ is that the SOFIE ablated influx has an elemental
134 breakdown consistent with that predicted by combining chemical ablation and solar system dust
135 models with observations [*Carrillo-Sánchez et al.*, 2020]. This in turn provides a straightforward

136 relationship between the ablated meteoric influx determined from SOFIE (see Section 5) and total
 137 meteoric influx (ablated plus surviving material).

Table 1. Relative abundance of the top five meteoric elements, for incoming meteoroids, and for the top three smoke compositions identified by SOFIE.

| Element | Ablated Influx ¹ (t d ⁻¹) | Influx Fraction ¹ (% by wt.) | Olivine ² Mg _{0.8} Fe _{1.2} SiO ₄ (% by wt.) | Magnesiowüstite ² Mg _{0.6} Fe _{0.4} O (% by wt.) | Wüstite ² FeO (% by wt.) |
|---------|---|--|--|---|---|
| Fe | 2.8 | 34 | 38 | 42 | 78 |
| O | 2.7 | 32 | 36 | 30 | 22 |
| Si | 1.2 | 14 | 16 | - | - |
| Mg | 1.0 | 12 | 11 | 27 | - |
| Na | 0.3 | 3 | - | - | - |

¹According to *Carrillo-Sanchez et al.* [2020].
²Identified using SOFIE smoke observations by *Hervig et al.* [2017a]. The detection probabilities were 68% for olivine, 75% for magnesiowüstite, and 71% for wüstite.

138 3. WACCM Model

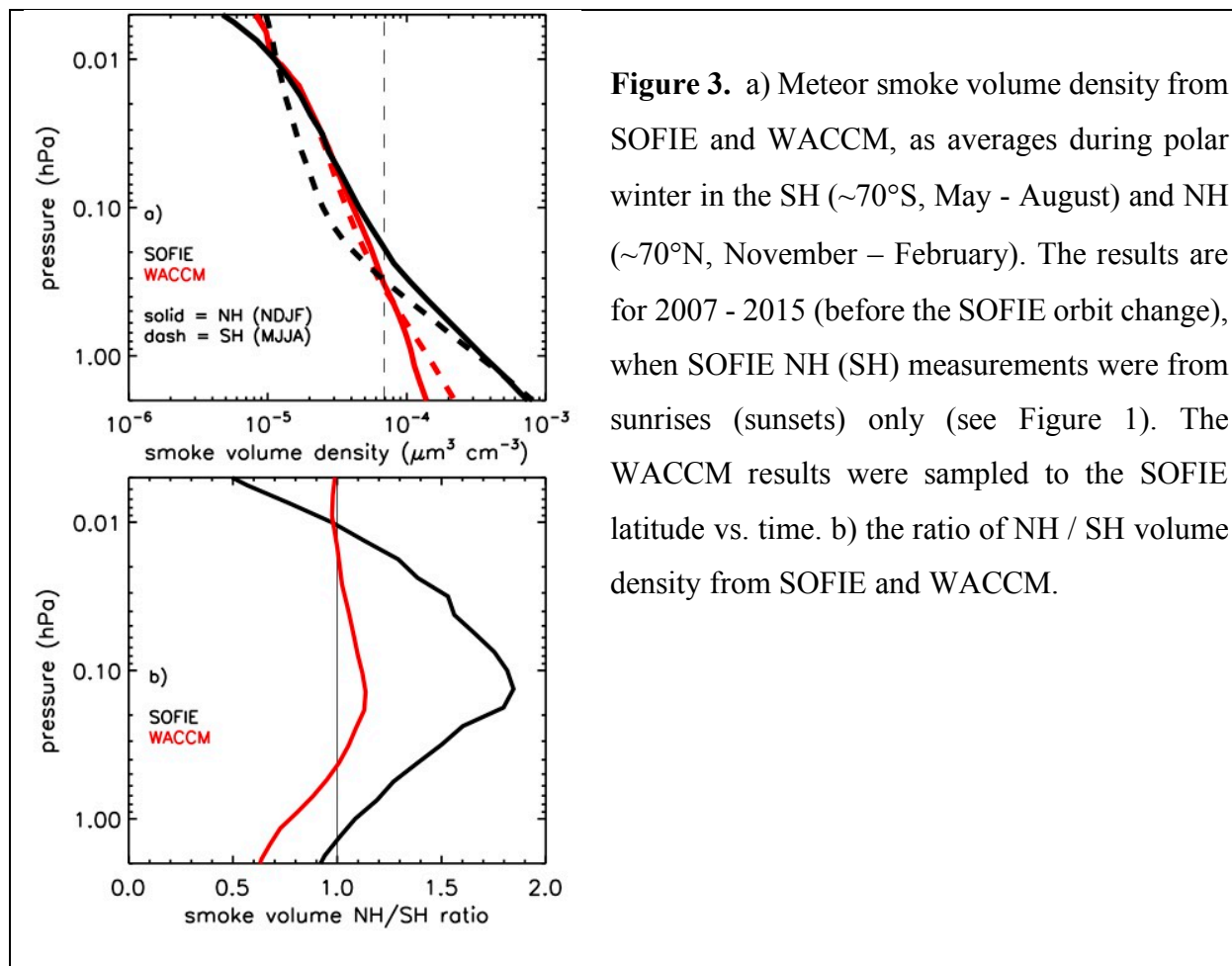
139 This work used a model description of meteoric smoke based on a first principles
 140 representation in the Whole Atmosphere Community Climate Model (WACCM), as originally
 141 described by *Bardeen et al.* [2008]. The model begins with meteoric ablation products as metal-
 142 rich molecular clusters of 0.25 nm radius, and simulates the evolution of smoke particles due to
 143 growth by agglomeration, sedimentation, and transport. The model includes annual and latitudinal
 144 variations in meteoric influx [*Fentzke et al.*, 2008], with the ablated meteoric influx (AMI)
 145 specified as the annual global mean. Note that the model only considers the ablated fraction of
 146 incoming meteoroids, since the surviving material falls quickly to the surface [*Plane et al.*, 2012].
 147 Later model adaptations used the original smoke component of *Bardeen et al.* [2008] incorporated
 148 in the specified dynamics (SD) version of WACCM [*Bardeen et al.*, 2010]. The smoke simulations
 149 were later integrated into NCAR Community Earth System Model (CESM) version of WACCM
 150 [*Marsh et al.*, 2013a; 2013b], along with new descriptions of the gas-phase chemistry of meteoric
 151 metals and interactions between smoke and trace gases [*Plane et al.*, 2015; *Frankland et al.*, 2015;

152 *James et al.*, 2017]. Finally, the model is nudged with the Modern-Era Retrospective Analysis for
153 Research and Applications (MERRA2) [*Molod et al.*, 2015; *Gelaro et al.*, 2017]. This is the
154 version used here, which is maintained at the University of Leeds, and was previously used in
155 comparisons with SOFIE by *Hervig et al.* [2017a]. WACCM results for 2007 - 2020 were used
156 here to determine daily zonal means which were sampled to the SOFIE latitude versus time.

157 **4. Meteoric Smoke**

158 The new SOFIE NH (sunrise) smoke V profiles are compared to SOFIE observations in
159 the SH (sunset) in Figure 3a, where the results are averages for winter months when smoke is
160 highest. The NH and SH observations are generally similar; however, note that SOFIE shows
161 greater extinction in the NH middle mesosphere. Results from WACCM are also shown in Figure
162 3a, where SOFIE is systematically greater than WACCM in the lower mesosphere ($P > \sim 0.5$ hPa).
163 This difference was explored by *Hervig et al.* [2017b], who found that it was consistent with a
164 layer of neutralized sulfate mixed with smoke at altitudes above the nominal sulfate layer during
165 autumn - winter, when temperatures are low. SOFIE indicates a larger hemispheric (NH vs. SH)
166 difference in the middle mesosphere ($\sim 0.2 - 0.01$ hPa) than is shown by WACCM. These
167 differences are further illustrated in Figure 3b, where the NH / SH V ratios are shown versus height.
168 This rendition shows that SOFIE and WACCM both indicate a similar height dependence in the
169 hemispheric difference, but that SOFIE differences ($\sim 65\%$ at 0.1 hPa) are much larger than
170 WACCM ($\sim 12\%$ at 0.1 hPa). The seasonal variation in smoke is largely driven by the global
171 mesospheric meridional circulation, where the polar winter maximum is due to transport of smoke
172 from across the globe. The larger hemispheric differences indicated by SOFIE could thus be the
173 result of a stronger circulation in the NH winter (or weaker in SH winter) than is contained in the
174 model. Another possibility is seasonal variability in the global meteoric input function. However,

175 the variation that is currently in WACCM, which is based on the dust sources at 1 AU in the solar
 176 system, indicates a very symmetric annual-average distribution with respect to latitude and season
 177 [Feng et al., 2013]. At pressures lower than ~0.01 hPa, SOFIE results are increasingly affected by
 178 noise, and the NH - SH differences at these heights are not taken seriously at this time.



179
 180 Time series of the new SOFIE sunrise (NH) smoke volume densities are compared to
 181 WACCM in Figure 4a, as the average V for 0.2 - 0.01 hPa (V'). The SOFIE - WACCM agreement
 182 is rather good, where both indicate similar annual variability and even a twin peak during winter.
 183 The exception is during winter 2013/14 where SOFIE V' is greater than in WACCM (Figure 4a),
 184 a difference that is currently not understood. The seasonal variation in smoke is shown in greater

185 detail in Figure 4b, where the annual time series are based on averages including 2007 - 2013.
 186 Recall that SOFIE smoke observations in summer are generally not useful due to contamination
 187 by PMCs. The agreement is very good concerning the timing and depth of the annual smoke
 188 variation, with the exception that WACCM shows a later start to the autumn - winter enhancement
 189 than SOFIE. This difference is most likely due to different timing of the seasonal transition in
 190 WACCM compared to the real atmosphere.

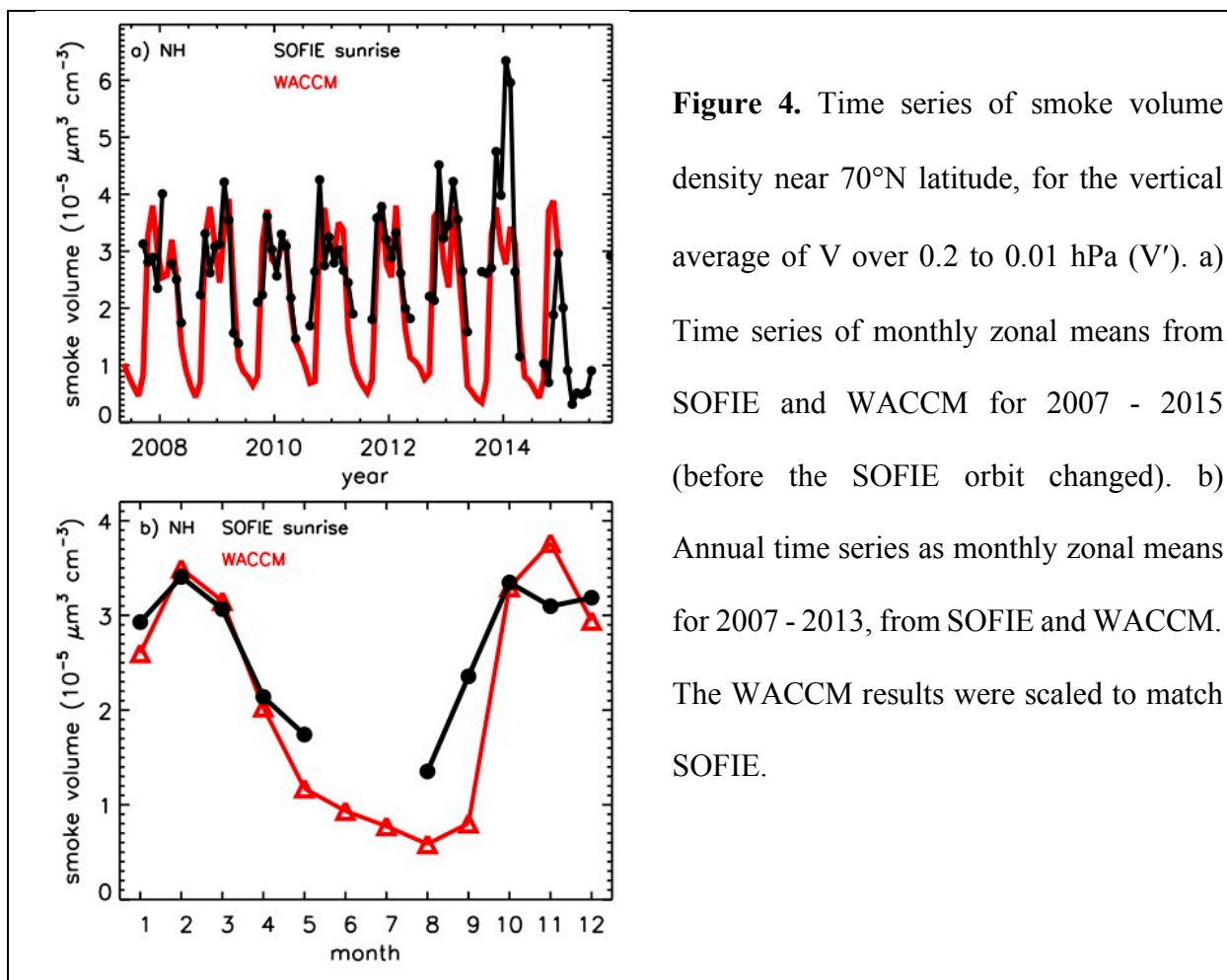


Figure 4. Time series of smoke volume density near 70°N latitude, for the vertical average of V over 0.2 to 0.01 hPa (V'). a) Time series of monthly zonal means from SOFIE and WACCM for 2007 - 2015 (before the SOFIE orbit changed). b) Annual time series as monthly zonal means for 2007 - 2013, from SOFIE and WACCM. The WACCM results were scaled to match SOFIE.

191
 192 The year-to-year smoke variations were examined further using winter averages. The
 193 latitude of SOFIE observations in winter was consistently near $\sim 70^\circ$ in both hemispheres, with the
 194 exception of 2017 - 2018 when lower latitudes were sampled due to the changing AIM orbit

195 (Figure 5a). The comparison of smoke V' (Figure 5b) highlights the hemispheric asymmetry
196 indicated by SOFIE (NH > SH), that is also present (although weaker) in WACCM (e.g., Figure
197 3). The SOFIE NH observations show greater interannual variations than the SH measurements,
198 which is consistent with greater variability in NH polar winter relative to the SH [*Schoeberl and*
199 *Newman, 2015*]. WACCM also shows greater year-to-year variability in the NH compared to the
200 SH, although variability in SOFIE is typically greater than in the model. Some of the interannual
201 variability is due to the changing SOFIE latitudes after 2017, and this is captured in WACCM
202 because the model was sampled to the SOFIE latitude vs. time. It is noteworthy, however, that
203 SOFIE indicates more smoke in the NH not only during 2007 - 2018 when the NH was observed
204 by sunrise occultations, but also in later years when the NH was observed by sunsets. This suggests
205 that the hemispheric asymmetry is not due to a bias between the sunrise and sunset operational
206 modes in SOFIE, but rather is a real characteristic of smoke in the mesosphere.

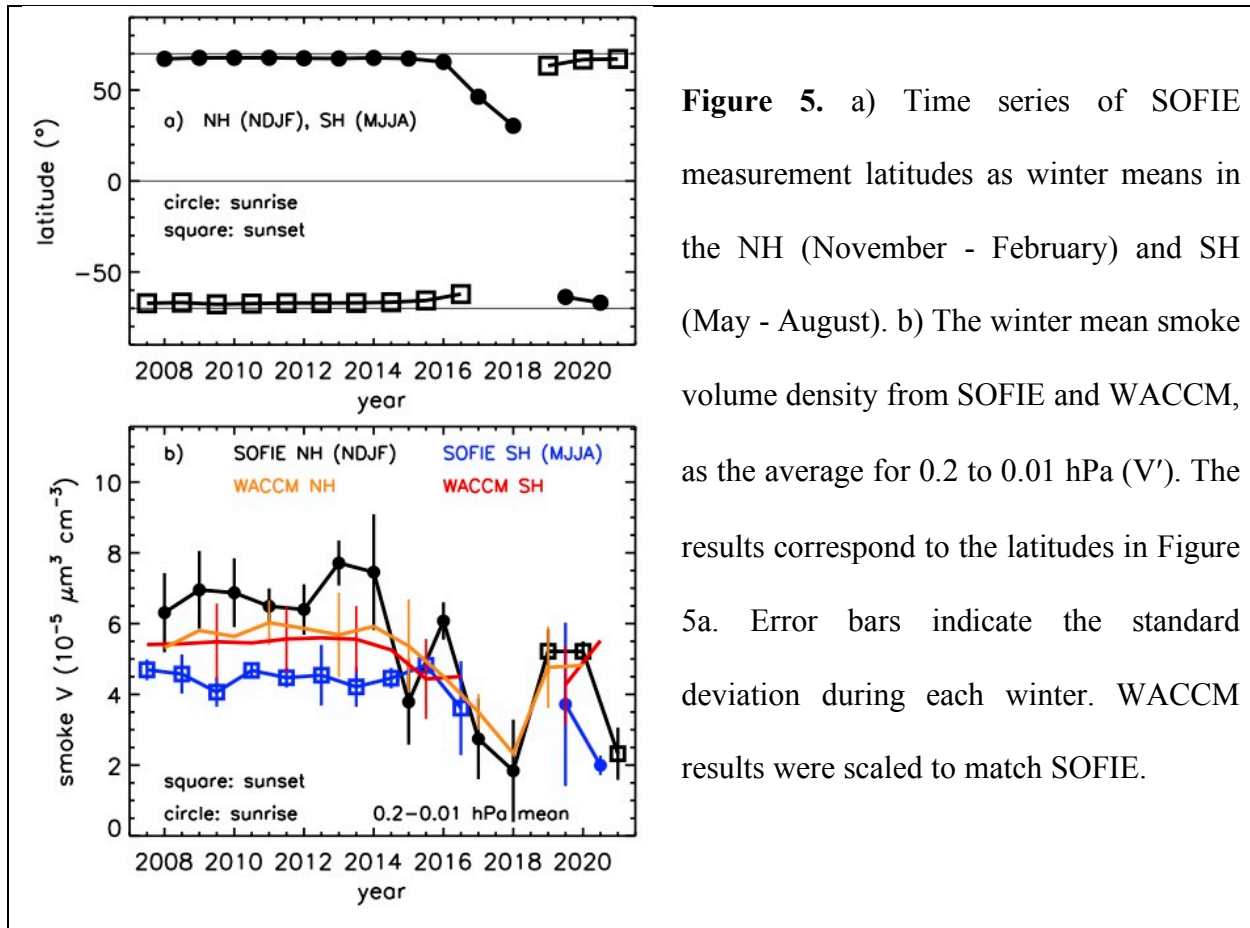


Figure 5. a) Time series of SOFIE measurement latitudes as winter means in the NH (November - February) and SH (May - August). b) The winter mean smoke volume density from SOFIE and WACCM, as the average for 0.2 to 0.01 hPa (V'). The results correspond to the latitudes in Figure 5a. Error bars indicate the standard deviation during each winter. WACCM results were scaled to match SOFIE.

207

208

209

210

211

212

213

214

215

216

217

The hemispheric difference in smoke was further explored by looking at water vapor in the upper mesosphere. Because H_2O behaves as a transport tracer and has a sharp vertical gradient in the mesosphere, it could indicate hemispheric differences that can confirm those in meteoric smoke. SOFIE and WACCM H_2O were examined as winter means in the upper mesosphere (0.2 - 0.01 hPa average, as for smoke). The results (Figure 6) show that there is less H_2O in the NH polar winter than in the SH polar winter, in both SOFIE and WACCM. *Lossow et al.* [2009] were the first to observe this hemispheric asymmetry in water vapor, and speculated that the underlying cause was differences in dynamics and diffusion. Water vapor decreases with height to very low values near the mesopause, so that descending air in the polar winter mesosphere causes seasonally low H_2O [Orsolini et al., 2010]. The hemispheric difference in winter H_2O is therefore suggestive

218 of stronger winter descent in the NH than the SH. This difference is qualitatively consistent with
 219 the hemispheric differences in smoke volume density (Figure 5b), where more smoke in the NH
 220 winter compared to the SH is indicative of stronger transport in the NH. Note that SOFIE and
 221 WACCM agree on the hemispheric differences in winter H₂O (SH is ~10% > NH), but that the
 222 magnitude of the hemispheric differences in smoke are much larger in SOFIE (20 to 80%) than in
 223 WACCM (<10%) (Figure 5b). Nevertheless, it is too simplistic to infer a one-to-one
 224 correspondence between different tracer profiles and pure advective transport, as noted by *Ryan et*
 225 *al.* [2018]. Other factors such as chemistry or diffusion need to be considered [*Smith et al.*, 2011],
 226 and it is reasonable to assume that these would behave differently for smoke and H₂O. Differences
 227 in any one of these factors between WACCM and the observations could explain the differences
 228 in the smoke and H₂O hemispheric asymmetries.

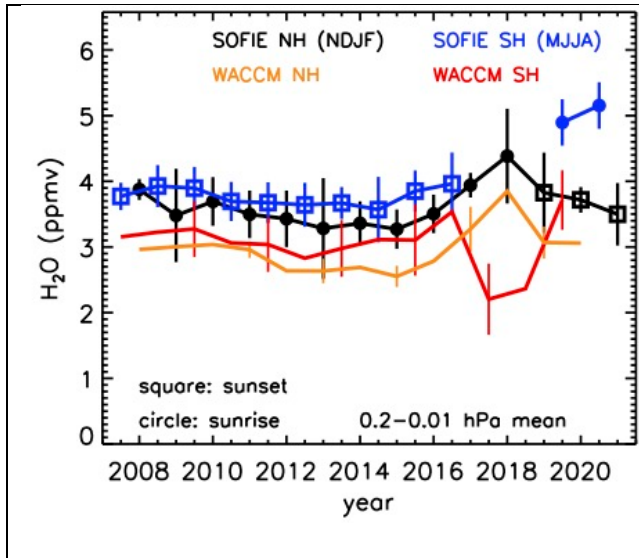


Figure 6. Time series of the winter mean water vapor from SOFIE and WACCM, as the average for 0.2 to 0.01 hPa. The results correspond to the latitudes in Figure 5a. Error bars indicate the standard deviation during each winter.

229 5. Meteoric Influx

230 Ablated meteoric influx (AMI) was derived through comparisons of SOFIE smoke volume
 231 density with WACCM runs conducted for different AMI values, as discussed in detail by *Hervig*
 232 *et al.* [2017a]. WACCM shows that when AMI is changed, smoke V changes by nearly the same

233 fractional amount at heights throughout the mesosphere. This is illustrated in Figures 7a - 7b,
234 where the modeled V' (average V for 0.2 - 0.01 hPa) is shown versus month and latitude from
235 WACCM runs with different AMI. The approach determines AMI vs. V' based on linear regression
236 to the model results, $AMI = A + B V'$, where A should be zero. WACCM results for AMI = 2, 8,
237 and 11 t d^{-1} were used in the regressions (Figures 7a and 7b), with the additional constraint that
238 the point ($V' = 0$, AMI = 0) was included to encourage A to approach zero. Values of A have only
239 small departures from zero ($< 3\%$), which reflect the uncertainties in the approach (not shown).
240 Because the SOFIE latitudes have changed over time (Figure 1), the regression to WACCM results
241 was carried out for monthly zonal means over a complete range in latitude. Values of B at polar
242 latitudes are found to change dramatically with season, with similar values during winter in both
243 hemispheres (Figures 7c - 7d). High values of B in summer occur because smoke is depleted due
244 to transport by the meridional circulation, while the regression was to the same annual global mean
245 AMI values. The results are also found to vary with latitude (Figure 7d), where the variation is
246 again driven by smoke transport. The uncertainties in derived MI are a combination of the SOFIE
247 observational errors ($\sim 9\%$ for monthly means), and the statistical uncertainty in the WACCM
248 representation of V' vs. AMI ($\sim 3\%$ in polar winter). The AMI uncertainties (δAMI) are the root-
249 sum-square of these terms, and the average δAMI for either hemisphere is $\sim 10\%$ during 2007 -
250 2021.

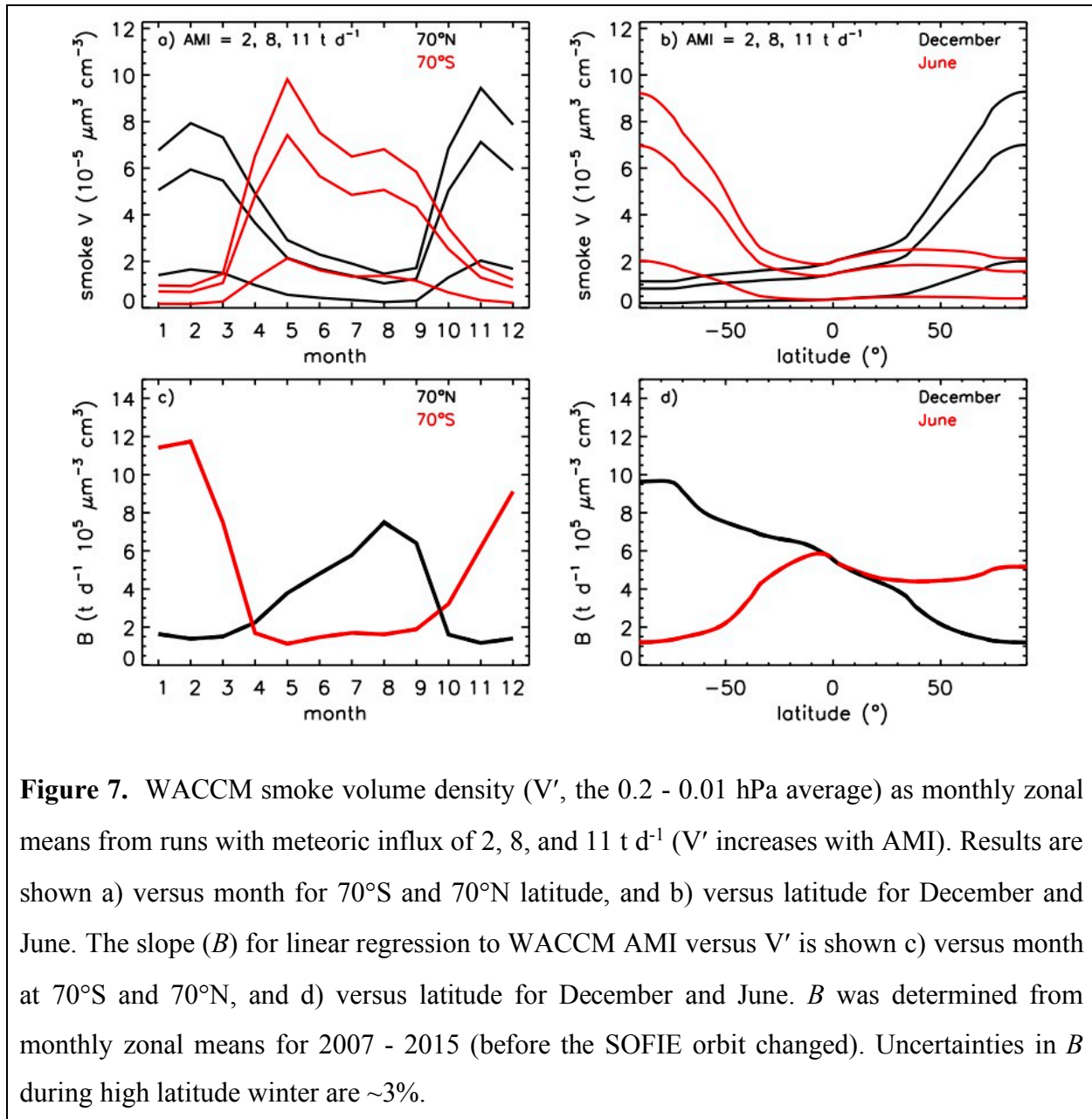


Figure 7. WACCM smoke volume density (V' , the 0.2 - 0.01 hPa average) as monthly zonal means from runs with meteoric influx of 2, 8, and 11 t d^{-1} (V' increases with AMI). Results are shown a) versus month for 70°S and 70°N latitude, and b) versus latitude for December and June. The slope (B) for linear regression to WACCM AMI versus V' is shown c) versus month at 70°S and 70°N, and d) versus latitude for December and June. B was determined from monthly zonal means for 2007 - 2015 (before the SOFIE orbit changed). Uncertainties in B during high latitude winter are $\sim 3\%$.

251

252

253

254

255

256

Ablated influx is shown versus month in Figure 8 during autumn through spring when meteoric smoke is most abundant (e.g., Figure 4b). The AMI estimates have additional errors during the transitional months when the SOFIE - WACCM agreement is poorer (e.g., September in the NH, see Figure 4b), although this is not captured in the current uncertainty estimates. Recall also that SOFIE smoke observations are typically not obtained in high latitude summer due to

257 signal contamination by PMCs. The results in Figure 8 are for 2007 - 2017 when sunrise (sunset)
 258 was in the NH (SH). The average NH AMI is ~30% greater than for the SH, which is statistically
 259 significant in terms of the AMI uncertainties (~10%). If SOFIE and WACCM contained the exact
 260 same seasonal variation in mesospheric smoke, however, then the AMI derived here should be
 261 constant throughout the year (by definition). Thus, the monthly variations in AMI can be
 262 interpreted as a byproduct of SOFIE - WACCM differences in the seasonal variation of smoke, as
 263 apparent in Figure 4b. The best AMI estimates from the SOFIE - WACCM comparisons will
 264 therefore be from multi-month averages, preferably during winter when smoke is elevated and
 265 relatively stable in time.

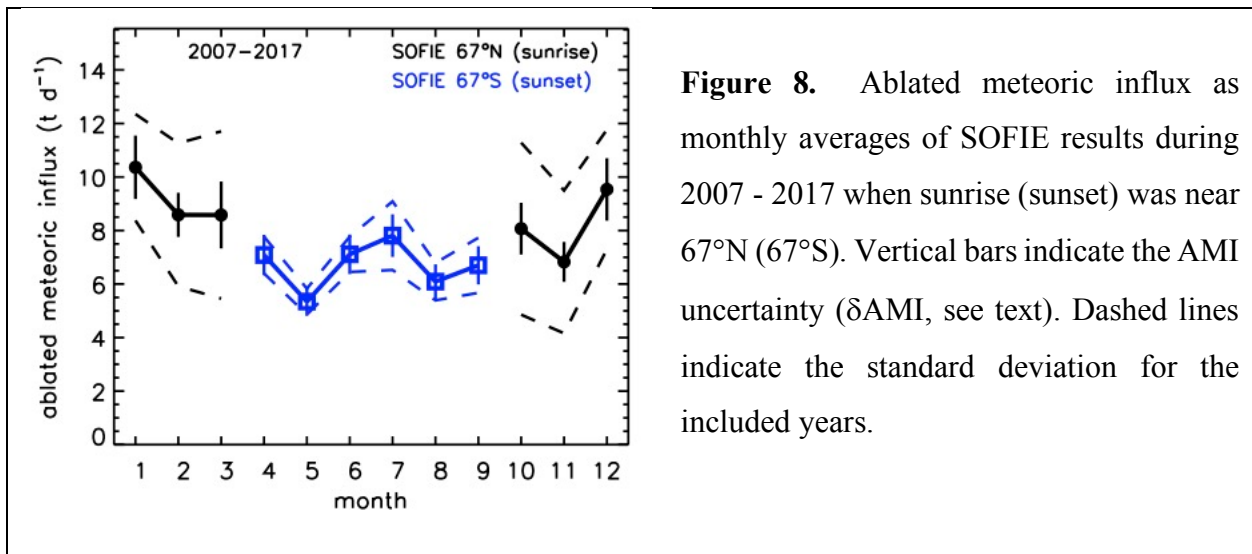


Figure 8. Ablated meteoric influx as monthly averages of SOFIE results during 2007 - 2017 when sunrise (sunset) was near 67°N (67°S). Vertical bars indicate the AMI uncertainty (δ AMI, see text). Dashed lines indicate the standard deviation for the included years.

266
 267 Ablated meteoric influx during 2007 - 2021 is shown as winter averages in both
 268 hemispheres in Figure 9, where the results are mostly for polar latitudes. AMI in the NH is typically
 269 greater than in the SH, with averages during 2007 - 2021 of $8.4 \pm 2.0 \text{ t d}^{-1}$ in the NH, and 6.2 ± 1.4
 270 t d^{-1} in the SH (\pm standard deviation of 14 years). For both hemispheres combined AMI is $7.3 \pm$
 271 2.0 t d^{-1} . The above standard deviations for 2007 - 2021 are ~22%, while the AMI uncertainty
 272 based on SOFIE and WACCM errors combined is ~10%, for either hemisphere. The results

273 indicate inter-annual variations in meteoric influx that are often statistically significant. Other
 274 observation of meteoric influx have shown year-to-year variability, including radars [e.g., *Janches*
 275 *et al.*, 2004] and satellite instruments [*Malaspina et al.*, 2016]. It is thus possible that the SOFIE
 276 inter-annual variations indicate real variability in meteoric influx, but this will be the topic of future
 277 studies.

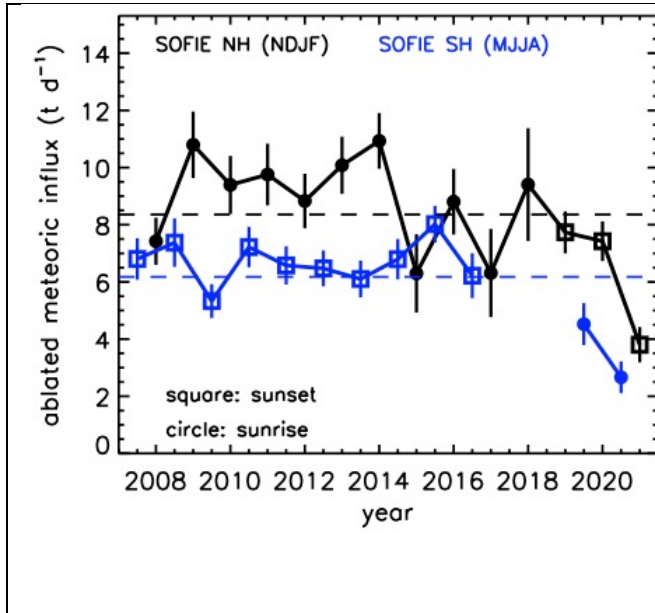


Figure 9. Time series of SOFIE AMI as winter means in the NH (November - February) and SH (May - August). The results correspond to latitudes as in Figure 5a. Note that sunrise (circle) and sunset (square) latitudes switched hemispheres in ~2018. The average AMI in the NH (8.4 t d⁻¹) and SH (6.2 t d⁻¹) are indicated by dashed lines. Error bars indicate the standard deviation for the included months.

278

279 The AMI derived here from the SOFIE-WACCM comparisons were anticipated to be equal
 280 in both hemispheres, yet hemispheric differences (NH > SH) exist during most years (Figure 9).
 281 This is due in part to hemispheric differences in SOFIE smoke volume density, that are weaker in
 282 WACCM (Figure 5b). Indeed, if WACCM had the same hemispheric differences in smoke V' as
 283 SOFIE, then the resulting AMI would be equal in both hemispheres. Biases between the SOFIE
 284 sunrise and sunset observational modes were dismissed because the hemispheric difference
 285 persists after 2018 when sunrise switched from the NH to SH (see Section 4). Transport in the
 286 model was dismissed because hemispheric differences in SOFIE and WACCM wintertime
 287 mesospheric H₂O are similar (Section 4). Another explanation could be a hemispheric asymmetry

288 in processes involving smoke microphysics (e.g., coagulation and sedimentation) and/or chemistry
289 (e.g., depletion of gas phase Fe by something other than smoke) that is incomplete in WACCM. A
290 final idea is suggested, which is that the hemispheric difference in SOFIE smoke is due to an
291 asymmetry in meteoric influx that is not included in WACCM. *Malaspina et al.* [2016] report
292 meteoric flux observations from the Wind satellite operating roughly 10^6 km from Earth, showing
293 a seasonal variation in MI with a maximum in March and a minimum in September. This annual
294 variation was traced to interstellar particles, which flow into the Earth's orbital direction in March.
295 These observations are not considered in the *Fentzke, et al.* [2008] description of meteoric influx
296 variations used in WACCM, and thus could be a component in the SOFIE - WACCM
297 disagreement concerning the hemispheric differences in mesospheric smoke.

298 The final consideration is derivation of total meteoric influx (TMI) from the SOFIE ablated
299 meteoric influx results. The present study treats meteoric smoke as Fe-rich olivine, which has an
300 elemental abundance nearly identical to that of the ablated meteoric source (see Section 2). As a
301 result, the conversion from AMI to TMI can be taken directly from the *Carrillo-Sánchez et al.*
302 [2020] results, which give $TMI / AMI = 28 \pm 16 \text{ t d}^{-1} / 8.3 \pm 4.7 \text{ t d}^{-1} = 3.4$. The resulting TMI
303 values from this work are $28.4 \pm 6.8 \text{ t d}^{-1}$ in the NH and $21.0 \pm 4.9 \text{ t d}^{-1}$ in the SH. For both
304 hemispheres combined TMI is $25.0 \pm 7.0 \text{ t d}^{-1}$. The stated uncertainties are the standard deviation
305 of the winter values for 2007 - 2021 (e.g., Figure 9). Note that the uncertainty in the SOFIE TMI
306 estimates reported above are the standard deviations over 14 years, and that the experimental errors
307 represent an additional 10% uncertainty. It is furthermore arguable that the SOFIE TMI
308 uncertainties could be increased due to propagation of the *Carrillo-Sánchez et al.* [2020] errors
309 (~57%).

310 **6. Summary**

311 An improved SOFIE sunrise signal calibration has produced meteoric smoke extinction
312 retrievals in the Northern Hemisphere, for the first time. The new observations are in good
313 agreement with WACCM simulations concerning both the time and height dependence of smoke
314 in the mesosphere. Comparing the SOFIE extinction measurements to WACCM requires
315 knowledge of the smoke composition, to describe the optical properties that relate extinction to
316 volume density. The present study assumes that smoke in the mesosphere exists purely as Fe-rich
317 olivine with the justification that 1) it is detected optically by SOFIE, 2) it has the same elemental
318 abundance of Fe, Mg and Si as predicted from meteoric ablation, and 3) it is anticipated by theory
319 and laboratory experiments [*Saunders and Plane, 2011*]. With the assumption of olivine, SOFIE
320 results indicate a global mean ablated meteoric influx of $7.3 \pm 2.0 \text{ t d}^{-1}$ (total influx of $25.0 \pm 7.0 \text{ t}$
321 d^{-1}), based on averages for both hemispheres during 2007 - 2021. The new SOFIE influx results
322 agree with *Carrillo-Sánchez et al. [2020]* (within 11%) who used models and observations to
323 derive an ablated influx of $8.3 \pm 4.7 \text{ t d}^{-1}$ (total influx of $28.0 \pm 16 \text{ t d}^{-1}$). This closure provides
324 further support for mesospheric smoke existing as olivine. Additionally, these new results
325 reconcile previous differences between SOFIE influx estimates from *Hervig et al. [2017a]* (AMI
326 = 3.3 t d^{-1} ; TMI = 30 t d^{-1}) and *Carrillo-Sánchez et al. [2016]* (AMI = 7.9 t d^{-1} ; TMI = 43 t d^{-1}).

327 Both SOFIE and WACCM show ~10% hemispheric differences in wintertime mesospheric
328 H₂O (SH > NH), that are consistent with stronger transport in the NH winter vs. the SH. This
329 difference in transport is also apparent in both the SOFIE and WACCM mesospheric smoke
330 results, which show less smoke in the SH polar winter compared to NH winter. The open issue is
331 that the hemispheric difference in smoke is greater in SOFIE (~36%) than in WACCM (~2%).
332 Because the meteoric influx estimates rely on comparisons of SOFIE and WACCM, a hemispheric

333 difference emerges in the SOFIE influx values (~30%). While this difference is close to the
334 combination of experimental uncertainties (~10%) and geophysical variability (~20%), it is
335 persistent in time and bears some thought. Sunrise - sunset biases in the SOFIE observations were
336 dismissed because the hemispheric difference persists after 2018 when sunrise switched from the
337 NH to SH (vice versa for sunset). Transport in WACCM was dismissed because the hemispheric
338 differences in H₂O are the same in WACCM and SOFIE. The parting ideas in this regard are
339 incomplete chemistry or microphysics in the smoke simulations, or asymmetries in meteoric influx
340 that are not represented in the model.

341 **Acknowledgements.** This work was funded in part by the AIM mission through NASA's Small
342 Explorers Program under contract NAS5-03132. The modeling work at the University of Leeds
343 was supported by the European Research Council (project number 291332 – CODITA). SOFIE
344 data are available online at sofie.gats-inc.com. The updated SOFIE extinctions used in this study
345 are available by contacting Mark Hervig (mark@gats-inc.com). The WACCM data sets generated
346 for this work have been archived at the Leeds University PETAL (PetaByte Environmental Tape
347 Archive and Library) <https://petal.leeds.ac.uk/>.

348 **References**

349 Bardeen, C. G., O. B. Toon, E. J. Jensen, D. R. Marsh, and V. L. Harvey (2008), Numerical
350 simulations of the three-dimensional distribution of meteoric dust in the mesosphere and upper
351 stratosphere, *J. Geophys. Res.*, *113*, D17202, doi:10.1029/2007JD009515.

352 Bardeen, C. G., O. B. Toon, E. J. Jensen, M. E. Hervig, C. E. Randall, S. Benze, D. R. Marsh, and
353 A. Merkel (2010), Numerical simulations of the three-dimensional distribution of polar
354 mesospheric clouds and comparisons with Cloud Imaging and Particle Size (CIPS)
355 experiment and the Solar Occultation For Ice Experiment (SOFIE) observations, *J. Geophys.*

356 *Res.*, 115, D10204, doi:10.1029/2009JD012451.

357 Carrillo-Sánchez, J. D., D. Nesvorný, P. Pokorný, D. Janches, and J. M. C. Plane (2016), Sources
358 of cosmic dust in the Earth's atmosphere, *Geophys. Res. Lett.*, 43,
359 doi:10.1002/2016GL071697.

360 Carrillo-Sánchez, J. D.; Gómez-Martín, J. C.; Bones, D. L.; Nesvorný, D.; Pokorný, P. Benna, M.;
361 Flynn, G. F.; Plane, J. M. C. (2020) Cosmic dust fluxes in the atmospheres of Earth, Mars,
362 and Venus, *Icarus*, 335, art. no. 113395.

363 Feng, W., Marsh, D. R., Chipperfield, M. P., Janches, D., Hoffner, J. Yi, F., and Plane, J. M. C.
364 (2013): A global atmospheric model of meteoric iron, *Journal of Geophysical Research*, 118,
365 9456–9474.

366 Fentzke, J.T., D. Janches, and J.J. Sparks (2008), Latitudinal and seasonal variability of the
367 micrometeor input function: A study using model predictions and observations from Arecibo
368 and PFISR, *J. Atmos. Solar-Terr. Phys.*, doi:10.1016/j.jastp.2008.07.015.

369 Frankland, V. L.; James, A. D.; Feng, W.; Plane, J. M. C. (2015): The uptake of HNO₃ on meteoric
370 smoke analogues, *Journal of Atmospheric and Solar-Terrestrial Physics*, 127, 150-160, 127,
371 150-160, doi: 10.1016/j.jastp.2015.01.010.

372 Gardner, C. S., Alan Z. Liu, D. R. Marsh, Wuhu Feng and J. M. C. Plane (2014), Inferring the
373 Global Cosmic Dust Influx to the Earth's Atmosphere from Lidar Observations of the Vertical
374 Flux of Mesospheric Na, *J. Geophys. Res. Space Physics*, DOI: 10.1002/2014JA020383.

375 Gordley, L. L., et al. (2009), The Solar Occultation For Ice Experiment (SOFIE), *J. Atmos. Sol.-*
376 *Terr. Phys.*, 71, 300-315, doi:10.1016/j.jastp.2008.07.012.

377 Gelaro, R., McCarty, W., Suárez, M. J., Todling, R., Molod, A., Takacs, L., Randles, C. A.,
378 Darmenov, A., Bosilovich, M. G., Reichle, R., Wargan, K., Coy, L., Cullather, R., Draper, C.,

379 Akella, S., Buchard, V., Conaty, A., da Silva, A. M., Gu, W., Kim, G., Koster, R., Lucchesi,
380 R., Merkova, D., Nielsen, J. E., Partyka, G., Pawson, S., Putman, W., Rienecker, M., Schubert,
381 S. D., Sienkiewicz, M., & Zhao, B. (2017). The Modern-Era Retrospective Analysis for
382 Research and Applications, Version 2 (MERRA-2), *Journal of Climate*, 30(14), 5419-5454,
383 <https://journals.ametsoc.org/view/journals/clim/30/14/jcli-d-16-0758.1.xml>.

384 Hervig, M. E., L. L. Gordley, L. E. Deaver, D. E. Siskind, M. H. Stevens, J. M. Russell III, S. M.
385 Bailey, L. Megner, and C. G. Bardeen (2009), First satellite observations of meteoric smoke
386 in the middle atmosphere, *Geophys. Res. Letters*, doi:10.1029/2009GL039737.

387 Hervig, M. E., Brooke, J. S. A., Feng, W., Bardeen, C. G., Plane, J. M. C. (2017a), Constraints on
388 meteoric smoke composition and meteoric influx using SOFIE observations with models, *J.*
389 *Geophys. Res. Atmospheres*, 122, doi:10.1002/2017JD027657.

390 Hervig, M. E., C. G. Bardeen, D. E. Siskind, M. J. Mills, R. Stockwell, (2017b), Meteoric smoke
391 and H₂SO₄ aerosols in the upper stratosphere and mesosphere, *Geophys. Res. Letters*, 44,
392 doi:10.1002/2016GL072049.

393 James, A. D., D. R. Moon, W. Feng, P. S. J. Lakey, V. L. Frankland, D. E. Heard, J. M. C. Plane
394 (2017), The uptake of HO₂ on meteoric smoke analogues, *J. Geophys. Res.*, 122, 554–565.

395 Janches, D., S. Palo, E. M. Lau, S. K. Avery, J. P. Avery, S. de la Peña, N. A. Makarov (2004),
396 Diurnal and seasonal variability of the meteor flux at the South Pole measured with radars,
397 *Geophys. Res. Lett.*, 31, doi:10.1029/2004GL021104.

398 Lossow, S., J. Urban, H. Schmidt, D. R. Marsh, J. Gumbel, P. Eriksson, and D. Murtagh (2009),
399 Wintertime water vapor in the polar upper mesosphere and lower thermosphere: First satellite
400 observations by Odin submillimeter radiometer, *J. Geophys. Res.*, 114, D10304,
401 doi:10.1029/2008JD011462.

402 Malaspina, D. M. and L. B. Wilson III (2016), A database of interplanetary and interstellar dust
403 detected by the Wind spacecraft, *J. Geophys. Res. Space Physics*, *121*, 9369–9377,
404 doi:10.1002/2016JA023209.

405 Marsh, D. R., Janches, D., Feng, W. and Plane, J. M. C. (2013a): A global model of meteoric
406 sodium, *J. Geophysical Research*, *118*, 11,442–11,452.

407 Marsh, D. R., M. J. Mills, D. E. Kinnison, J. F. Lamarque, N. Calvo, and L. M. Polvani (2013b),
408 Climate Change from 1850 to 2005 Simulated in CESM1(WACCM), *J. Clim.*, *26*, 7372-7391.

409 Megner, L, D. E. Siskind, M. Rapp, and J. Gumbel (2008), Global and temporal distribution of
410 meteoric smoke; a 2D simulation study, *J. Geophys. Res.*, *113*, D03202,
411 doi:10.1029/2007JD009054.

412 Molod, A., Takacs, L., Suarez, M., and Bacmeister, J.: Development of the GEOS-5 atmospheric
413 general circulation model: evolution from MERRA to MERRA2, *Geosci. Model Dev.*, *8*,
414 1339–1356, <https://doi.org/10.5194/gmd-8-1339-2015>, 2015.

415 Orsolini, Y. J., Urban, J., Murtagh, D. P., Lossow, S., and Limpasuvan, V. (2010), Descent from
416 the polar mesosphere and anomalously high stratopause observed in 8 years of water vapor
417 and temperature satellite observations by the Odin Sub-Millimeter Radiometer, *J. Geophys.*
418 *Res.*, *115*, D12305, doi:10.1029/2009JD013501.

419 Plane, J. M. C. (2012), Cosmic dust in the earth’s atmosphere, *Chem. Soc. Rev.*, *41*, 6507-6518,
420 doi: 10.1039/c2cs35132c.

421 Plane, J. M. C., W. Feng; Dawkins, E. C. M. (2015): The Mesosphere and Metals: Chemistry and
422 Changes, *Chemical Reviews*, *115*, 4497 - 4541, doi: 10.1021/cr500501m.

423 Russell, J. M. III, et al. (2009), Aeronomy of Ice in the Mesosphere (AIM): Overview and early
424 science results, *J. Atmos. Sol.-Terr. Phys.*, *71*, 289-299, doi:10.1016/j.jastp.2008.08.011.

425 Ryan, N. J., Kinnison, D. E., Garcia, R. R., Hoffmann, C. G., Palm, M., Raffalski, U., and Notholt,
426 J. (2018): Assessing the ability to derive rates of polar middle-atmospheric descent using trace
427 gas measurements from remote sensors, *Atmos. Chem. Phys.*, *18*, 1457–1474,
428 <https://doi.org/10.5194/acp-18-1457-2018>.

429 Saunders, R.W. and J. M. Plane (2011), A photo-chemical method for the production of olivine
430 nanoparticles as cosmic dust analogues, *Icarus*, *212*, 373-382, ISSN 0019-1035,
431 [10.1016/j.icarus.2010.12.019](https://doi.org/10.1016/j.icarus.2010.12.019).

432 Schoeberl, M.R., and P.A. Newman (2015), Encyclopedia of Atmospheric Sciences (Second
433 Edition), *Academic Press*, 2015, Pgs 12-17, ISBN 9780123822253,
434 <https://doi.org/10.1016/B978-0-12-382225-3.00228-0>.

435 Smith, A. K., R. R. Garcia, D. R. Marsh, and J. H. Richter (2011), WACCM simulations of the
436 mean circulation and trace species transport in the winter mesosphere, *J. Geophys. Res.*, *116*,
437 D20115, doi:10.1029/2011JD016083.